

## Article

# CFD Analysis of the Heat Transfer and Fluid Flow Characteristics Using the Rectangular Rib Attached to the Fin Surface in a Solar Air Heater

Hwi-Ung Choi <sup>1</sup> , Kwang-Am Moon <sup>2</sup>, Seong-Bhin Kim <sup>2</sup> and Kwang-Hwan Choi <sup>3,\*</sup>

<sup>1</sup> Industry-University Cooperation Foundation, Pukyong National University, Busan 48513, Republic of Korea; nopoil@naver.com

<sup>2</sup> Graduate School of Refrigeration and Air-Conditioning Engineering, Pukyong National University, Busan 48513, Republic of Korea; topo6785@pukyong.ac.kr (K.-A.M.); tjdqsls2274@pukyong.ac.kr (S.-B.K.)

<sup>3</sup> Department of Refrigeration and Air-Conditioning Engineering, Pukyong National University, Busan 48513, Republic of Korea

\* Correspondence: choikh@pknu.ac.kr

**Abstract:** This study discussed the effect of ribbed fin, which was suggested by the authors, on the enhancement of heat transfer and flow characteristics of fluid in a solar air heater. The ribbed fin has a rectangular rib at the base and side surfaces of the fin. Thus, it can increase the heat transfer coefficient in the fluid field of a solar air heater as well as extend the heat transfer area. The simulation was performed with various Reynolds numbers, relative heights, and pitches of the rib. The presence of the rib enhances the heat transfer performance by 3.497 times over a smooth fin. However, the addition of the rib also increases pressure drop. Thus, the thermo-hydraulic performance, which considers both heat transfer enhancement and pressure drop increase, was also discussed. Furthermore, this study developed correlations for the Nusselt number and friction factor as a function of geometric condition of the rib and Reynolds number. The correlations accurately predicted the Nusselt number for the base and side surfaces of the fin and friction factor with mean absolute percent errors of 4.24%, 4.53%, and 7.33%, respectively.

**Keywords:** solar thermal energy; solar collector; solar air heater; Nusselt number; friction factor; CFD



**Citation:** Choi, H.-U.; Moon, K.-A.; Kim, S.-B.; Choi, K.-H. CFD Analysis of the Heat Transfer and Fluid Flow Characteristics Using the Rectangular Rib Attached to the Fin Surface in a Solar Air Heater. *Sustainability* **2023**, *15*, 5382. <https://doi.org/10.3390/su15065382>

Academic Editor: Jifeng Song

Received: 13 February 2023

Revised: 7 March 2023

Accepted: 14 March 2023

Published: 17 March 2023



**Copyright:** © 2023 by the authors. Licensee MDPI, Basel, Switzerland. This article is an open access article distributed under the terms and conditions of the Creative Commons Attribution (CC BY) license (<https://creativecommons.org/licenses/by/4.0/>).

## 1. Introduction

The solar air heater (SAH), which can directly convert incident solar radiation into useful thermal energy without any environmental pollution, is one of the most promising solar energy conversion systems. This system can be used for various purposes, such as space heating, drying fruit and crops, and curing products in domestic and industrial fields. A further advantage of the SAH is its low manufacturing, operating, and maintenance costs due to its simple design compared to other solar thermal systems [1]. However, since air has a low thermal conductivity, the absorber is unable to effectively transfer heat to flowing air, resulting in low thermal efficiency of the system [2]. To overcome this issue, many researchers have employed various techniques.

One of the most effective methods to enhance the thermal efficiency of the SAH is improving the convective heat transfer coefficient in a fluid field of an SAH. There are several methods that can be utilized to improve the convective heat transfer coefficient, including the use of ribs, baffles, obstacles, etc. [3]. Yadav and Bhagoria [4–6] investigated the effect of transverse circular, square, and equilateral triangular ribs on the heat transfer enhancement using 2D CFD (computational fluid dynamics) analysis and reported that the ribs located under the absorber could enhance convective heat transfer coefficient in a fluid field of an SAH. Gawande et al. [7] evaluated the heat transfer enhancement and pressure drop increase using the reverse L-shaped transverse rib in an SAH with various relative pitches and Reynolds number ( $Re$ ). This research showed that the presence of

an L-shaped rib improved heat transfer by 2.827 times. Singh and Singh [8] analyzed the heat transfer improvement and increment in pressure drop in an SAH using non-uniform cross-section rib with various roughness pitches and  $Re$  using 3D CFD analysis. This study showed that the Nusselt number ( $Nu$ ) and friction factor ( $f$ ) were enhanced to a maximum of 2.18 and 3.34, respectively. Singh et al. [9] compared two different ribs, namely multiple broken transverse rib and square wave-shaped rib, for thermal performance improvement of the SAH using CFD methodology. They presented that the multiple broken rib has better thermal performance and a lower pressure drop than the square wave-shaped rib. Choi and Choi [10] suggested installing a transverse triangle obstacle at the bottom side of the air channel and found that the addition of the obstacle could enhance heat transfer performance by 3.37 times over a smooth air channel. Kumar and Goel [11] examined how the cross-sectional shape of the roughness affects the thermal characteristics of an SAH with a triangular duct. A total of six different shapes were chosen as roughness geometries, and the forward chamfered rectangular rib has the best thermal–hydraulic performance. Alam and Souayah [12] evaluated the thermo-hydraulic characteristics of a solar air tube with a dimple with various relative heights and pitches of dimple, tube length, and  $Re$ . They presented that the presence of artificial roughness on the tube led to an enhancement in  $Nu$  by 5.12 times over smooth tube. Haldar et al. [13] suggested SAH roughened with continuous wavy rib and reported that the suggested rib had a maximum value of thermo-hydraulic performance (THP) of 1.96 under the investigated conditions. Singh et al. [14] analyzed the performance of SAH using a multi-V rib and double-pass single-flow air duct and presented that the roughened double-pass single-flow SAH has 2.37 times higher thermal efficiency than that of smooth double-pass single-flow SAH.

The other method is extending the heat transfer area. A natural convection SAH with a finned absorber was experimented by Pakdaman et al. [15]. This study reported that the 20% improvement in heat transfer performance could be achieved by a 66% increase in the heat transfer area. Fudholi et al. [16] investigated the effect of a fin on the thermal efficiency of a double-pass SAH and reported that adding a fin could increase thermal efficiency by 9%. Yang et al. [17] developed a numerical model for the SAH integrated with an offset strip fin and investigated the thermal performance of the SAH with various parameters such as transparent cover properties, stagnant air layer height, and insulation thickness. The thermo-hydraulic performance of SAH integrated with a wavy finned absorber was studied with various fin spacing and air mass flow rates by Priyam and Chand [18]. This study concluded that the wavy finned absorber could improve thermohydraulic efficiency by 35.83% over the plane SAH. Kabeel et al. [19] experimentally investigated the influence of longitudinal fin height on SAH's daily thermal efficiency. Their study showed that the higher fin height resulted in higher daily thermal efficiency of SAH due to increased heat transfer area. Kansara et al. [20] compared three different SAH: SAH with an empty channel, SAH with a fin, and SAH with porous media. This research indicated that the SAH with porous media performed better than SAH with an empty channel or a fin. Chand et al. [21] proposed the SAH integrated with louvered fins and experimentally evaluated its thermal performance. This study showed that the louvered fins were able to enhance thermal efficiency by 106.7% as compared to plane SAH. Nagaraj et al. [22] investigated the thermo-hydraulic efficiency of double-pass SAH integrated with aerofoil fins by experiment and CFD simulation. This study reported that the optimum configuration of aerofoil fins provided 20.94% higher efficiency than that of single-pass SAH.

In the literature review above, however, it was seen that improving the thermal efficiency of SAH mainly focused on either extending the heat transfer area or enhancing the heat transfer coefficient. In addition, the improvement of SAH's efficiency by extending the heat transfer area or enhancing the heat transfer coefficient has been individually carried out, and there have been very limited studies that utilize heat transfer techniques that take into account both extension of the heat transfer area and improvement in heat transfer coefficient at the same time in SAH. In this research, a longitudinal fin combined with a rectangular rib, named ribbed fin, was suggested. The ribbed fin has a rectangular rib at the

base and side surfaces of the fin. Hence, unlike previous methods, it is capable of increasing the heat transfer coefficient as well as the area of heat transfer in a fluid field of an SAH. In the current investigation, a CFD analysis was employed to confirm how the addition of the rib at the base and side surfaces of the fin affects heat transfer and fluid flow within a fluid field of an SAH. The enhancement in heat transfer and fluid flow characteristics were investigated with various relative heights and pitches of the rib and  $Re$  for the fixed width and height of the fin to confirm the effect of the geometric condition of the rib. Moreover, the correlations for  $Nu$  and  $f$ , which can be used to predict the thermal efficiency and blowing power of an SAH, were developed as a function of relative height, relative pitch, and  $Re$ .

## 2. Methodology

### 2.1. Description of the Model

Figure 1 shows the schematics of an SAH combined with a ribbed fin. The fins are installed under the absorber of an SAH, and rectangular ribs are attached to the base and side surfaces of the fins.

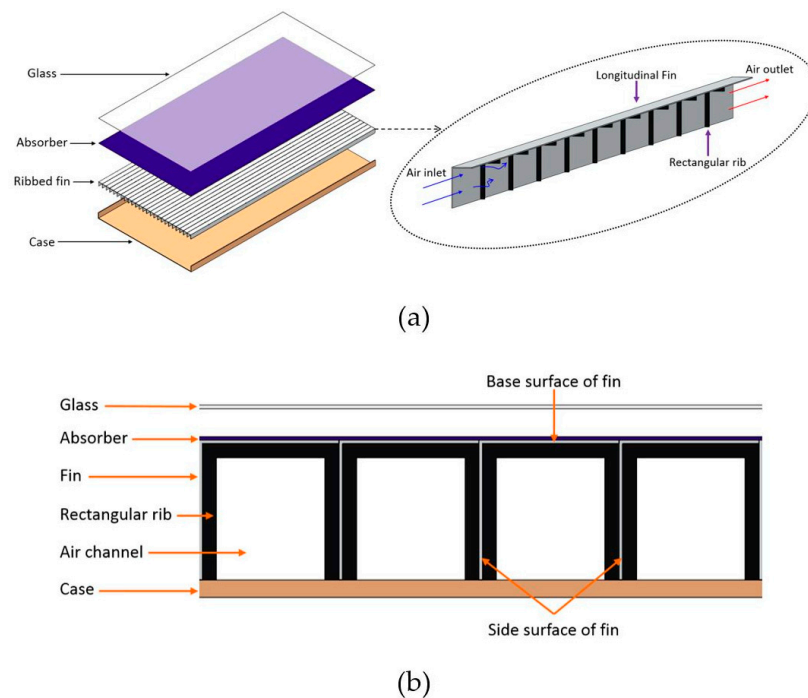


**Figure 1.** Schematic of proposed SAH with ribbed fin: (a) exploded view, (b) front view.

In this study, the CFD analysis was conducted for one air channel among several air channels divided by the fins. A symmetric boundary condition was applied to the center of the air channel and the side surface of the fin to reduce the solution domain. Figure 2 presents the solution domain used for CFD analysis and a schematic view of the domain with boundary conditions. The solution domain comprises an entrance region, a test section with a ribbed fin, and an exit region. The length of the entrance region, test section, and exit region was 120 mm, 1000 mm, and 60 mm, respectively.

In the current investigation, the heat transfer enhancement and characteristics of fluid flow were investigated for various relative heights and pitches of the rectangular rib for a fixed height and width of a fin. The relative heights and pitches were in the range of 0.04 to 0.28 and 10 to 34, respectively. An evaluation of each configuration was conducted using five different  $Re$  ranging from 3000 to 15,000. Table 1 lists the geometric conditions of the solution domain and the parameters investigated in this study.

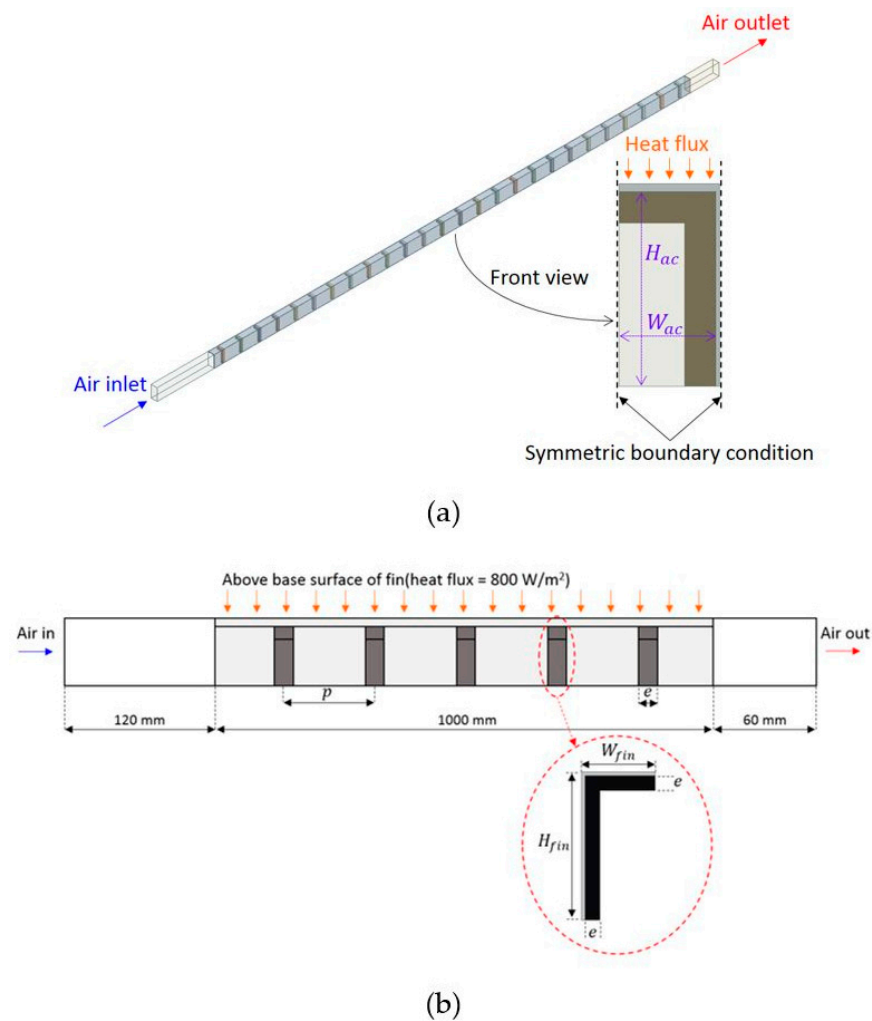


**Figure 2.** Solution domain of SAH: (a) 3D model, (b) schematics of the domain.

**Table 1.** Geometric conditions of the solution domain and range of parameters.

| Parameter       |                            | Value                            |
|-----------------|----------------------------|----------------------------------|
| Air channel     | Height (mm), $H_{ac}$      | 24                               |
|                 | Width (mm), $W_{ac}$       | 12                               |
| Fin             | Height (mm), $H_{fin}$     | 25                               |
|                 | Width (mm), $W_{fin}$      | 12.5                             |
|                 | Thickness (mm)             | 1                                |
| Rectangular rib | Relative height (–), $e/D$ | 0.04, 0.1, 0.16, 0.22, 0.28      |
|                 | Relative pitch (–), $p/e$  | 10, 18, 26, 34                   |
|                 | Reynolds number (–), $Re$  | 3000, 6000, 9000, 12,000, 15,000 |

## 2.2. Boundary Condition

As mentioned above, the symmetric boundary condition was appointed at the center of the air channel and the fin's side surface. A constant heat flux of  $800 \text{ W/m}^2$  was introduced on the base surface of the fin. In addition, an adiabatic wall condition was used for the other surfaces. All of the solid surfaces were assumed to have the no-slip boundary condition. For the inlet boundary condition, a uniform air velocity was chosen with a fixed air temperature of 300 K, and a pressure of 101,325 Pa was chosen as an outlet boundary condition. The boundary conditions employed in the simulation can be found in Table 2.

**Table 2.** Boundary conditions.

| Boundary                            | Conditions  |
|-------------------------------------|-------------|
| Inlet velocity (m/s)                | 1.83–9.13   |
| Reynolds number (–)                 | 3000–15,000 |
| Outlet pressure (Pa)                | 101,325     |
| Top surface of the fin ( $W/m^2$ )  | 800         |
| Side surface of the solution domain | Symmetric   |
| Other walls                         | Adiabatic   |

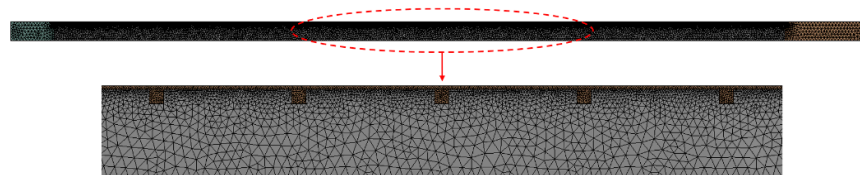
### 2.3. Grid Generation and Independence

In this study, the ANSYS Fluent 17.1 was employed to solve the governing equations and analyze heat transfer and flow characteristics in the SAH with a ribbed fin. The 3D model was prepared in ANSYS design modeler and meshed non-uniformly using ANSYS ICEM CFD. For grid independent test, the cell number varied from 1,167,142 to 7,296,861.

In Table 3, the  $Nu$  at the base surface of the fin ( $Nu_{base}$ ),  $Nu$  at the side surfaces of the fin ( $Nu_{side}$ ), and the  $f$  for a fixed  $Re$  of 9000 with the relative height and pitch of 0.04 and 10 were presented with the various numbers of cells. As shown in the table, after 5,998,181 cells, the further increase in the cell number results in a change of less than 1% in  $Nu$  and  $f$ . Consequently, 5,998,181 cells were selected as the appropriate cell number for the simulation. Figure 3 presents the solution domain meshed with the selected number of cells.

**Table 3.** Variation in Nusselt number and friction factor.

| Number of Cell | $Nu_{base}$ (–) | Change in $Nu_{base}$ (%) | $Nu_{side}$ (–) | Change in $Nu_{side}$ (%) | $f$ (–) | Change in $f$ (–) |
|----------------|-----------------|---------------------------|-----------------|---------------------------|---------|-------------------|
| 1,167,142      | 33.687          | –                         | 39.577          | –                         | 0.0262  | –                 |
| 3,690,883      | 32.965          | 2.192                     | 37.007          | 6.945                     | 0.0247  | 5.823             |
| 4,691,223      | 31.933          | 3.232                     | 37.544          | 1.432                     | 0.0248  | 0.046             |
| 5,998,181      | 32.377          | 1.373                     | 38.030          | 1.277                     | 0.0251  | 1.355             |
| 7,296,861      | 32.382          | 0.014                     | 38.299          | 0.703                     | 0.0252  | 0.498             |

**Figure 3.** Solution domain meshed with selected cell number.

### 2.4. Solution Method

In the current investigation, the heat transfer enhancement and fluid flow characteristics of a 3D solution domain were analyzed using the Ansys Fluent 17.1. The aforementioned boundary conditions were applied to the solution domain in order to solve the simulation model. The second-order upwind scheme is employed for the discretization of all equations, and the coupled algorithm is employed to link pressure and momentum equations. The convergence criteria values for energy and other equations were set to be  $10^{-6}$  and  $10^{-4}$ , respectively.

### 2.5. Turbulence Model

For the purpose of selecting a turbulence model, the  $Nu_{base}$ ,  $Nu_{side}$ , and  $f$  with smooth fin surface were evaluated with four different turbulence models, including standard  $k-\epsilon$  with enhanced wall treatment, Realizable  $k-\epsilon$  with EWT, RNG  $k-\epsilon$  with EWT, and SST  $k-\omega$  model. A comparison was made between the simulated results and those obtained from Gnielinski correlation and Dittus-Boelter empirical correlation, both of which have been

widely employed in related research [8,23–25]. The Gnielinski and Dittus–Boelter empirical correlations are expressed as Equations (1) and (2).

$$Nu_s = \frac{(f_g/8)(Re - 1000)Pr}{1 + 12.7(f_g/8)^{1/2}(Pr^{2/3} - 1)} \text{ for } 3000 < Re < 10,000 \quad (1)$$

$$Nu_s = 0.023Re^{0.8}Pr^{0.4} \text{ for } 10,000 < Re \quad (2)$$

where  $f_g$  is friction factor for Gnielinski correlation and is calculated from Equation (3).

$$f_g = (0.79 \ln Re - 1.64)^{-2} \quad (3)$$

The friction factor for smooth air channel ( $f_s$ ) in an SAH was calculated from the modified Blasius equation and is obtained from Equation (4) [9,26–28].

$$f_s = 0.085Re^{-0.25} \quad (4)$$

Figure 4 exhibits the  $Nu_{base}$  and  $Nu_{side}$  obtained from CFD simulation with the values obtained from the Gnielinski and Dittus–Boelter correlation.

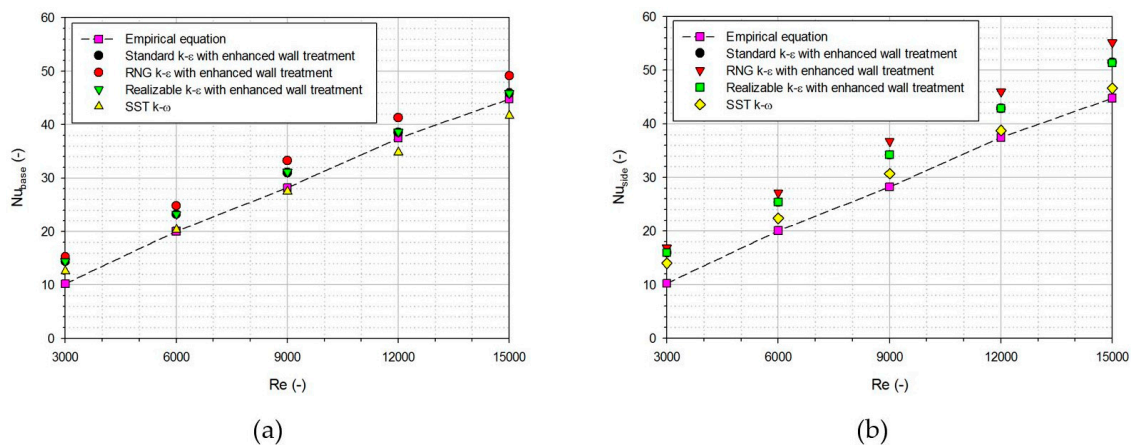


**Figure 4.** Comparison of  $Nu$  obtained from CFD analysis by different turbulent models and the values of empirical correlation: (a) base surface (b) side surface.

The results show that the SST  $k-\omega$  model has the lowest MAPEs of 12.96%, 8.18%, and 4.94% for  $Nu_{base}$ ,  $Nu_{side}$  and  $f_s$ , respectively, among the investigated turbulence model. Thus, the SST  $k-\omega$  model was employed as a turbulence model for further analysis, which was also used by other researchers [12,29–31].

## 2.6. Performance Indicators

This study focuses on the enhancement in heat transfer and a rise in pressure drop caused by the rectangular rib attached to the fin surface. As the heat is transferred from the fin's base and side surfaces to the flowing air, the  $Nu_{base}$  and  $Nu_{side}$  were obtained and are, respectively, calculated from the Equations (5) and (6).

$$Nu_{base} = \frac{h_{base}D}{k_{air}} \quad (5)$$

$$Nu_{side} = \frac{h_{side}D}{k_{air}} \quad (6)$$

where  $h_{base}$ ,  $D$ ,  $k_{air}$ , and  $h_{side}$  are convective heat transfer coefficient at the fin's side surface, hydraulic diameter of an air channel, thermal conductivity of air, and convective heat

transfer coefficient at the fin's base surface. The heat transfer coefficients for base and side surfaces were calculated using Equations (7) and (8).

$$h_{base} = \frac{\dot{Q}_{base}}{A_{base}(T_{base} - T_{air})} \quad (7)$$

$$h_{side} = \frac{\dot{Q}_{side}}{A_{side}(T_{side} - T_{air})} \quad (8)$$

where  $\dot{Q}_{base}$ ,  $A_{base}$ ,  $T_{base}$ ,  $T_{air}$ ,  $\dot{Q}_{side}$ ,  $A_{side}$ , and  $T_{side}$  are heat transfer rate from the fin's base surface to the flowing air, area of the fin's base surface, temperature of fin's base surface, temperature of flowing air, heat transfer rate from the fin's side surface to the flowing air, area of the fin's side surface, and temperature of fin's side surface, respectively.

The average value of Nusselt number between the ribbed fin and flowing air was calculated using the Equation (9).

$$Nu_{avg} = \frac{h_{avg}D}{k_{air}} \quad (9)$$

where  $h_{avg}$  is average convective heat transfer coefficient between ribbed fin and flowing air. The total heat transfer from the fin to the flowing air is equal to the sum of the heat transfer from the base and side surfaces of the fin, and can be expressed as Equation (10) [32].

$$\dot{Q}_{tot} = h_{avg}A_{tot}(T_{avg} - T_{air}) = \dot{Q}_{base} + \dot{Q}_{side} \quad (10)$$

where the  $A_{tot}$  and  $T_{avg}$  are the total area of the fin ( $A_{base} + A_{side}$ ) and the average temperature of the fin's base and side surfaces, respectively. From Equation (10), the  $h_{avg}$  can be derived as Equation (11).

$$h_{avg} = \frac{h_{base}A_{base}(T_{base} - T_{air}) + h_{side}A_{side}(T_{side} - T_{air})}{A_{tot}(T_{avg} - T_{air})} \quad (11)$$

where the  $A_{base}$  and  $A_{side}$  are the areas of the fin's base and side surfaces, respectively.

The average friction factor, which represents the pressure drop caused by the addition of the rib, was calculated from Equation (12).

$$f_{avg} = \frac{(\Delta P/L_{ac})D}{2\rho_{air}V_{air}^2} \quad (12)$$

where  $\Delta P$ ,  $\rho_{air}$ , and  $V_{air}$  are pressure drop along the air channel, air density, and velocity.

The addition of the rib on the fin's base and side surfaces can enhance the heat transfer performance. However, it also results in a notable increase in pressure drop. Hence, thermo-hydraulic performance (THP) was proposed by Webb and Eckert [33], which has been widely used by other researchers [4–6,9,24,25,34], to consider both improved heat transfer and rise in pressure drop caused by the addition of the rib. The value of THP was obtained from Equation (13).

$$THP = \frac{Nu_{avg}/Nu_s}{(f_{avg}/f_s)^{1/3}} \quad (13)$$

where the  $Nu_{avg}/Nu_s$  and  $f_{avg}/f_s$  represent heat transfer enhancement and an increase in friction factor by the rib, respectively. The higher value of THP indicates that the enhancement of heat transfer is higher at the same pressure drop.

### 3. Results and Discussion

#### 3.1. Heat Transfer

This section investigates the effect of the rib on the heat transfer enhancement in an SAH under different geometric and flow conditions. Figure 5 shows the  $Nu_{base}$  and  $Nu_{side}$  with various relative heights and pitches of the rib as a function of  $Re$ . From the figure, it was observed that the heat is more effectively transferred from the fin to the flowing air by incorporating the rectangular rib into the base and side surfaces of the fin. It can be also seen that the value of  $Nu_{side}$  is higher than that of  $Nu_{base}$  for a given geometric condition of the rib and  $Re$ . This is because, as the bottom side of an air channel has no rib, air flow near the side surface has less resistance than the air flow near the base surface.

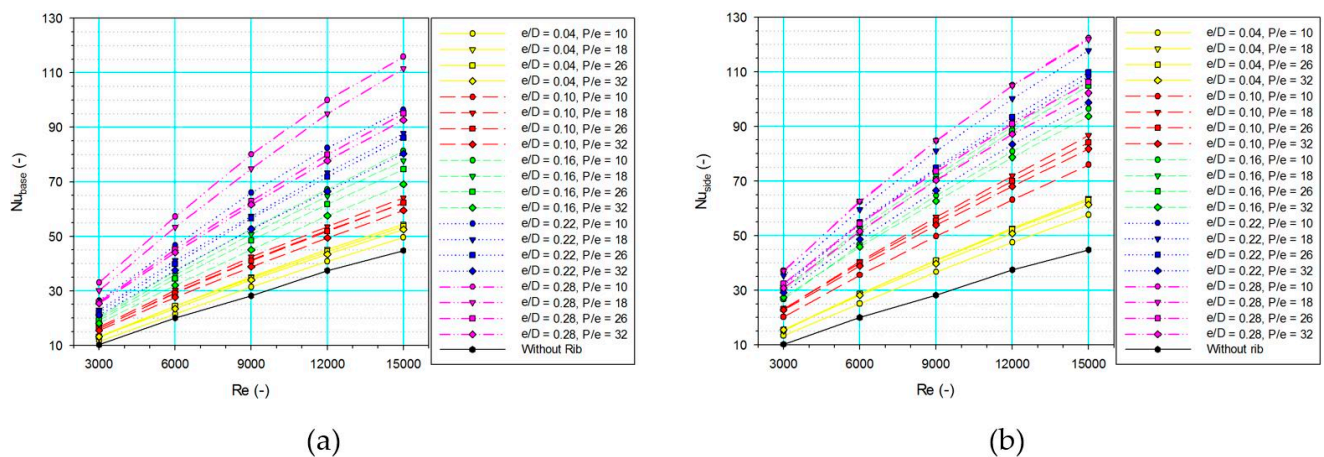


Figure 5.  $Nu$  with various geometric conditions of the rib and  $Re$ : (a) base surface (b) side surface.

Figure 6 presents the  $Nu_{avg}$  with relative height, relative pitch, and  $Re$ . The  $Nu_{avg}$  for ribbed fin varies between 12.77 to 120.19 according to the geometric condition of the rib and  $Re$ , whereas the  $Nu_{avg}$  for smooth fin ranges from 10.23 to 44.8. The  $Nu_{avg}$  is of an increasing trend with an increase in  $Re$  for all cases. This is because the higher  $Re$  leads to higher turbulent intensity due to an augmentation in turbulence kinetic energy in the fluid field, as presented in Figure 7.

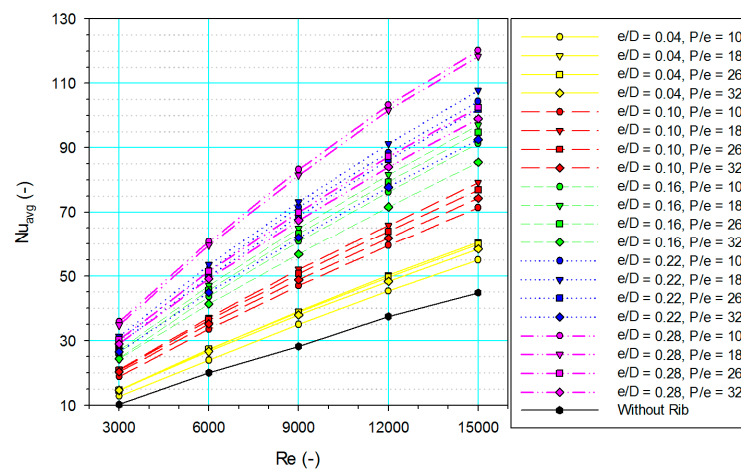
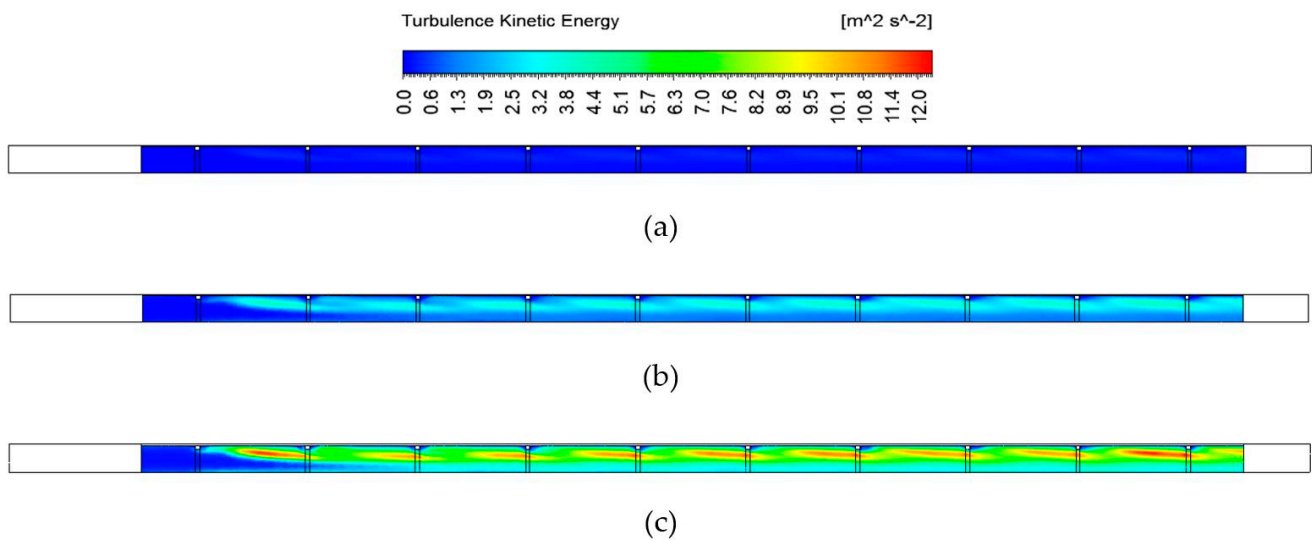
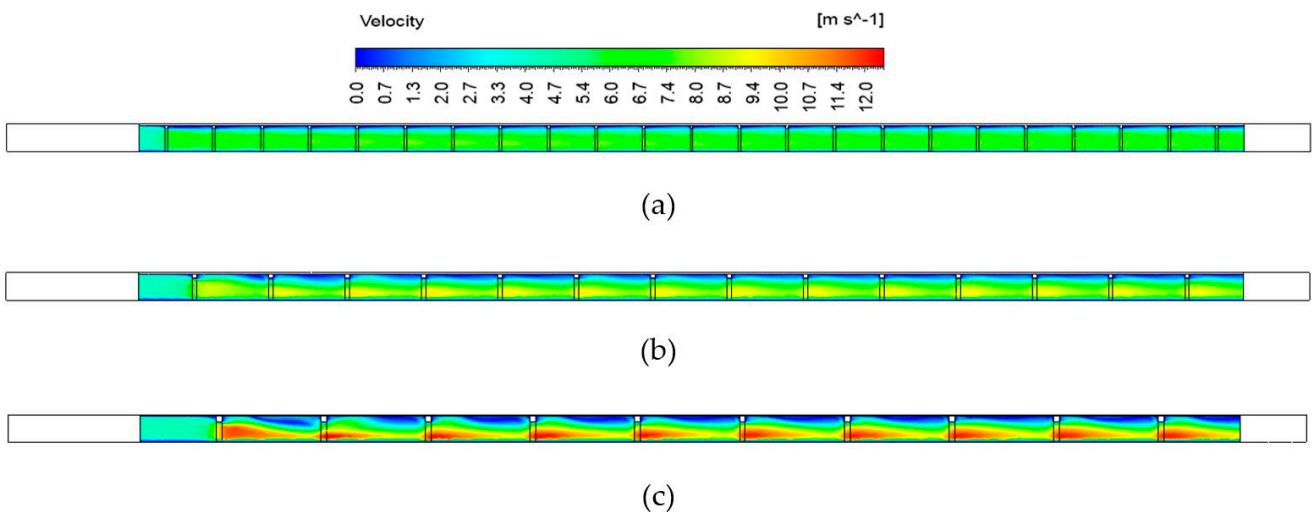


Figure 6.  $Nu_{avg}$  with various geometric conditions of the rib and  $Re$ .



**Figure 7.** Contours of turbulence kinetic energy for a fixed relative height of 0.16 and pitch of 26 at  $Re$  of (a) 3000, (b) 9000, and (c) 15,000.

The  $Nu_{avg}$  is improved with an increment in relative height for a fixed relative pitch and  $Re$ . This is attributed to the increase in air velocity in a fluid field, which increases heat transfer performance. Figure 8 shows the velocity contour for a fixed relative pitch of 18 and  $Re$  of 6000 with different relative heights. From the figure, it was observed that the higher relative height of the rib results in higher velocity in a fluid field of an SAH, as expected.



**Figure 8.** Velocity contours for a fixed relative pitch of 18 and  $Re$  of 6000 at the relative height of (a) 0.10, (b) 0.16, and (c) 0.22.

Figure 9 presents the  $Nu_{avg}$  as a function of relative pitch. In the figure, it was also observed that the  $Nu_{avg}$  tend to increase and then decrease as the relative pitch increases. Hence, there is an optimal relative pitch of the rib that maximizes heat transfer enhancement for a fixed relative height. The relative pitch, which maximizes the  $Nu_{avg}$ , was 26 for the  $Re$  from 3000 to 6000 and 18 for  $Re$  more than 9000 for a relative height of 0.04. In the case of relative heights of 0.1, 0.16, and 0.22, the optimal relative pitch was 18 regardless of  $Re$ , whereas, for the relative height of 0.28, the optimal value of a relative pitch was 10. It has also been confirmed that a relative pitch greater than 26 is unsuitable as a geometric condition of the ribs in heat transfer.

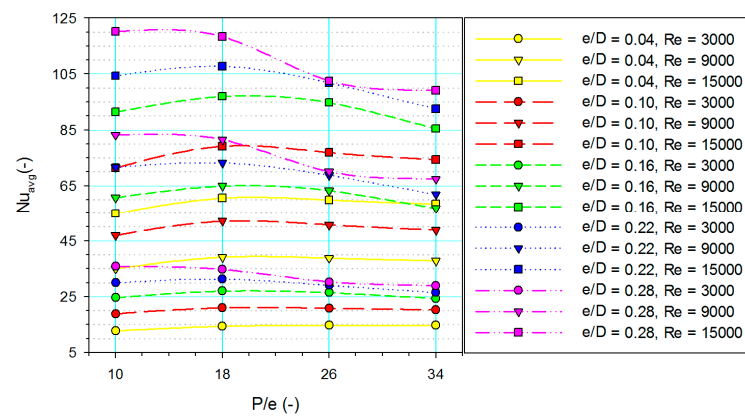


Figure 9.  $Nu_{avg}$  as a function of relative pitch.

Figure 10 shows the enhancement in  $Nu_{avg}$  through the addition of the rib at the fin surface of an SAH. It was found that the  $Nu_{avg}$  enhanced between 1.19 and 3.497, and the maximum enhancement occurred when the relative height, pitch, and  $Re$  were 0.28, 10, and 3000, respectively.

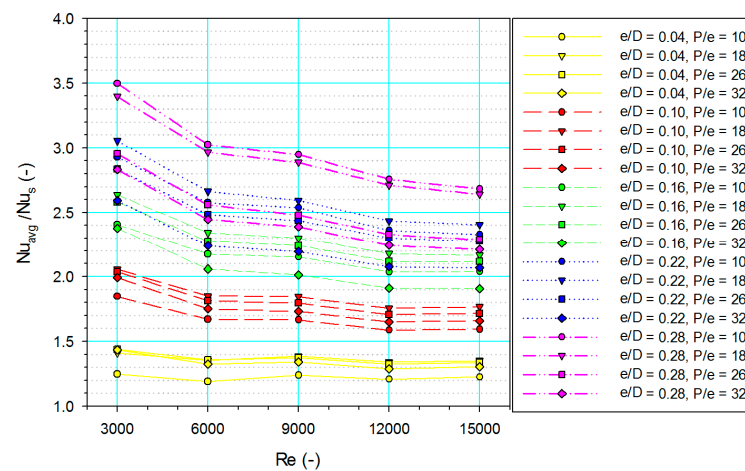


Figure 10. Enhancement in  $Nu_{avg}$ .

### 3.2. Flow Friction

This section demonstrates the  $f_{avg}$  through the installation of a rectangular rib at the fin surface of an SAH. Figure 11 shows the  $f_{avg}$  with various geometric conditions of the rib and  $Re$ . The  $f_{avg}$  for the ribbed fin ranges from 0.0179 to 0.2911 depending on the geometric condition of the rib and  $Re$ . In all cases, the presence of a rectangular rib increases the  $f_{avg}$  because the rectangular rib obstructs the flow.

The  $f_{avg}$  maintains similar values regardless of the  $Re$  for a given relative height and pitch of the rib. Generally,  $f_{avg}$  is proportional to the pressure drop and inversely proportional to the square of the velocity, as can be seen in Equation (12). Hence, from the above results, it can be seen that the increase in pressure drop and the increase in the square of the velocity were almost similar when the  $Re$  increased. In addition, the  $f_{avg}$  significantly increased with an increment in the relative height of the rectangular rib for a given relative pitch and  $Re$ . The reason for this is that the higher relative height in the air channel leads to more interruptions in the air flow path. As relative pitch increases for a fixed relative height and  $Re$ , the  $f_{avg}$  is declined owing to a reduction in the number of rectangular ribs. However, the effect of relative height was found to be more significant than those of relative pitch and  $Re$ . Figure 12 presents the enhancement in  $f_{avg}$ . The minimum enhancement in  $f_{avg}$  was found to be 1.709 when the relative height, pitch, and  $Re$  were 0.04, 34, and 3000,

respectively, while the maximum enhancement in  $f_{avg}$  was 85.597 when the relative height, pitch, and  $Re$  were 0.28, 10, and 15,000, respectively.

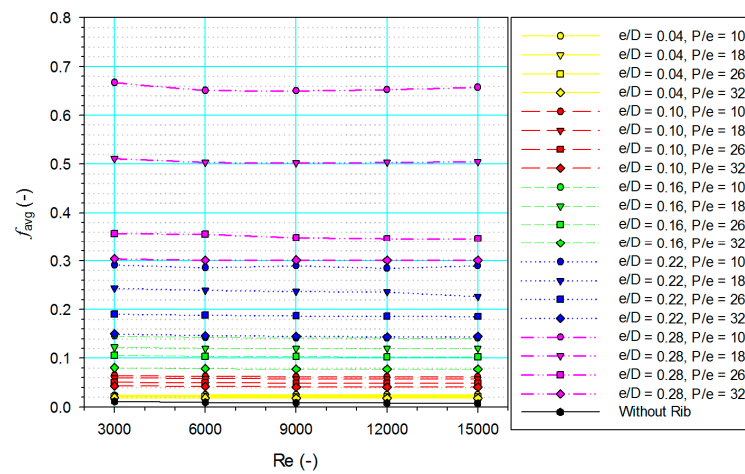


Figure 11.  $f_{avg}$  with various geometric conditions of rib and  $Re$ .

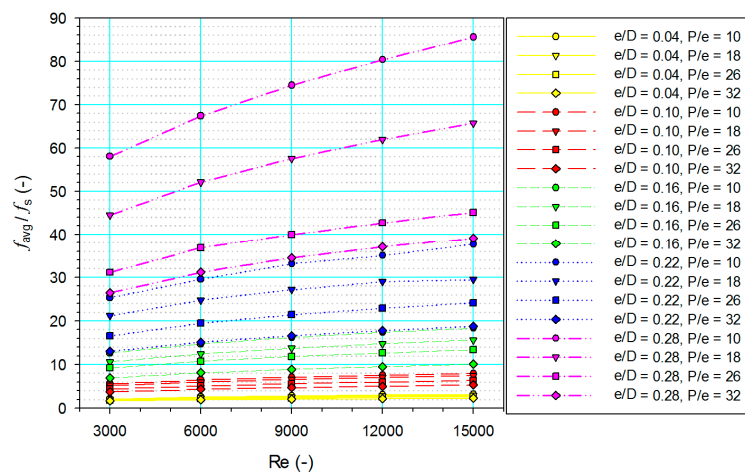


Figure 12. Enhancement in  $f_{avg}$ .

### 3.3. Thermo-hydraulic Performance

As discussed in the above section, adding a rectangular rib on the fin surface enhances heat transfer performance in a fluid field of an SAH. However, the presence of the rib also results in a notable rise in pressure drop. Thus, the THP is evaluated in this section, which takes into account both heat transfer enhancement and an increment in pressure drop.

Figure 13 shows THP with various geometric conditions of the rib and  $Re$ . The THP was in the range of 0.609 to 1.279. The THP increases with increasing relative pitch and decreasing  $Re$ . Hence, the higher relative pitch and lower  $Re$  are considered to be more effective for the SAH in terms of HTP. The THP increase and then decrease with an increment in relative height for a fixed relative pitch at  $Re$  of 3000. When the  $Re$  is in the range of 6000 to 15,000, the THP decrease as the relative height increase. The maximum THP was found when the relative height, pitch, and  $Re$  were 0.10, 34, and 3000, respectively.

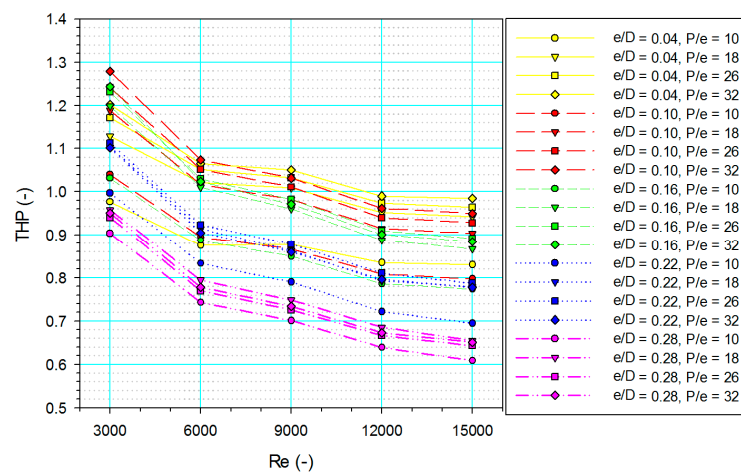


Figure 13. THP with various geometric conditions of the rib and  $Re$ .

#### 4. Development of Correlation

The development of correlations for  $Nu$  and  $f$  will be helpful in predicting the thermal performance and power consumption of an SAH and obtaining the necessary parameters for its design, since the correlations for  $Nu$  and  $f$  are important factors in the mathematical modeling of the SAH as can be found in many related studies [14,35–38]. Hence, in this section, the correlations are developed using the simulation results to predict  $Nu_{base}$ ,  $Nu_{side}$  and  $f_{avg}$ . These values are strongly affected by relative height, relative pitch, and  $Re$ . Therefore, the  $Nu_{base}$ ,  $Nu_{side}$  and  $f_{avg}$  can be expressed as Equations (14)–(16).

$$Nu_{base} = \text{function of } (Re, e/D, p/e) \tag{14}$$

$$Nu_{side} = \text{function of } (Re, e/D, p/e) \tag{15}$$

$$f_{avg} = \text{function of } (Re, e/D, p/e) \tag{16}$$

Generally, the relationship between  $Nu_{base}$  and  $Re$  can be expressed as Equation (17).

$$Nu_{base} = X_1 Re^n \tag{17}$$

Equation (17) can be rewritten as Equation (18).

$$\ln(Nu_{base}) = \ln(X_1) + n \ln(Re) \tag{18}$$

To find the value of  $n$ , the  $\ln(Nu_{base})$  was plotted as a function of  $\ln(Re)$  in Figure 14.

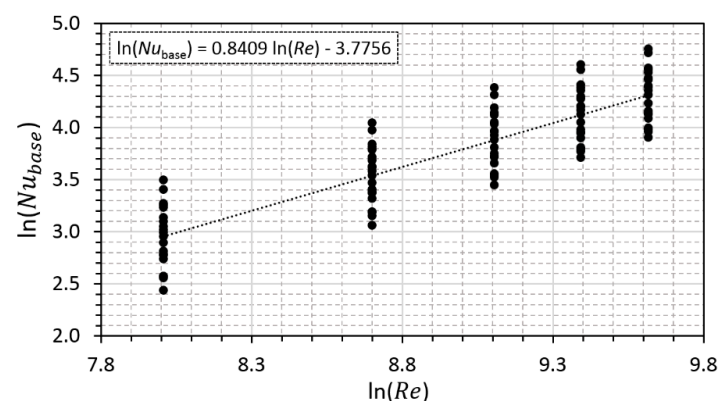


Figure 14. Plot of  $\ln(Nu_{base})$  with corresponding values of  $\ln(Re)$ .

In the figure, the value of  $n$ , which represents the slope of a line, is found to be 0.8409. Hence, Equation (17) can be expressed as Equation (19).

$$Nu_{base} = X_1 Re^{0.8409} \quad (19)$$

The coefficient  $X_1 (= Nu_{base}/Re^{0.8409})$  is a function of the relative height and pitch of a rectangular rib. Figure 15 presents the  $\ln(X_1)$  with  $\ln(e/D)$ .

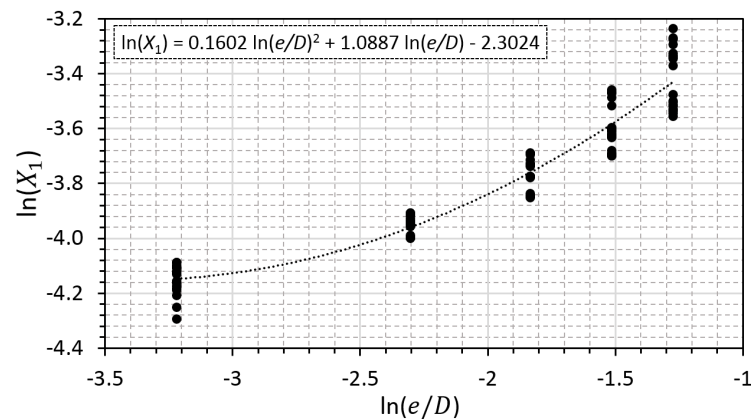


Figure 15. Plot of  $\ln(X_1)$  with corresponding values of  $\ln(e/D)$ .

The  $X_1$  and  $e/D$  were found to have the best relationship when expressed as a polynomial of the second-order equation. The relationship between  $X_1$  and  $e/D$  is expressed as Equation (20).

$$\ln(X_1) = \ln(X_2) + 1.0887 \ln(e/D) + 0.1602[\ln(e/D)]^2 \quad (20)$$

The above equation can be rearranged as Equation (21).

$$X_1 = X_2 (e/D)^{1.0887} \exp[0.1602[\ln(e/D)]^2] \quad (21)$$

The Equation (21) can be rewritten as Equation (22).

$$Nu_{base} = X_2 Re^{0.8409} (e/D)^{1.0887} \exp[0.1602[\ln(e/D)]^2] \quad (22)$$

The  $X_2 (= Nu_{base}/\{Re^{0.8409}(e/D)^{1.0887} \exp[0.1602[\ln(e/D)]^2]\})$  is a function of the relative pitch. The value of  $\ln(X_2)$  was plotted against  $\ln(p/e)$  in Figure 16.

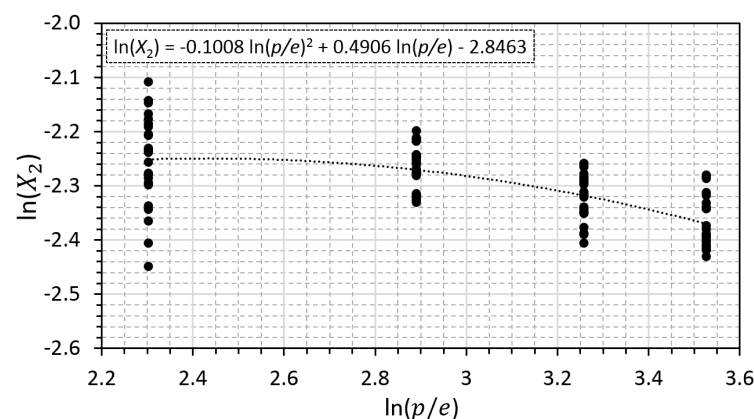


Figure 16. Plot of  $\ln(X_2)$  with corresponding values of  $\ln(p/e)$ .

Similar to the  $X_1$ , the  $X_2$  can be written as Equation (23).

$$X_2 = X_3 (p/e)^{0.4906} \exp[-0.1008[\ln(p/e)]^2] \quad (23)$$

Thus, Equation (22) can be rewritten as Equation (24).

$$Nu_{base} = X_3 Re^{0.8409} (e/D)^{1.0887} \exp[0.1602[\ln(e/D)]^2] (p/e)^{0.4906} \exp[-0.1008[\ln(p/e)]^2] \quad (24)$$

Here, the  $X_3$  is the constant value, which can be determined from the results in Figure 16. The  $X_3$  was found to be 0.05806; therefore, the final equation for  $Nu_{base}$  can be written as Equation (25).

$$Nu_{base} = 0.05806 Re^{0.8409} (e/D)^{1.0887} (p/e)^{0.4906} \exp[0.1602[\ln(e/D)]^2] \exp[-0.1008[\ln(p/e)]^2] \quad (25)$$

Figure 17 illustrates a comparison between the predicted values of  $Nu_{base}$  obtained from the developed correlation and the results from the CFD simulation. As shown in the figure, the majority of the predicted values are within the deviation limit of 12.5% with a MAPE of 4.24%.

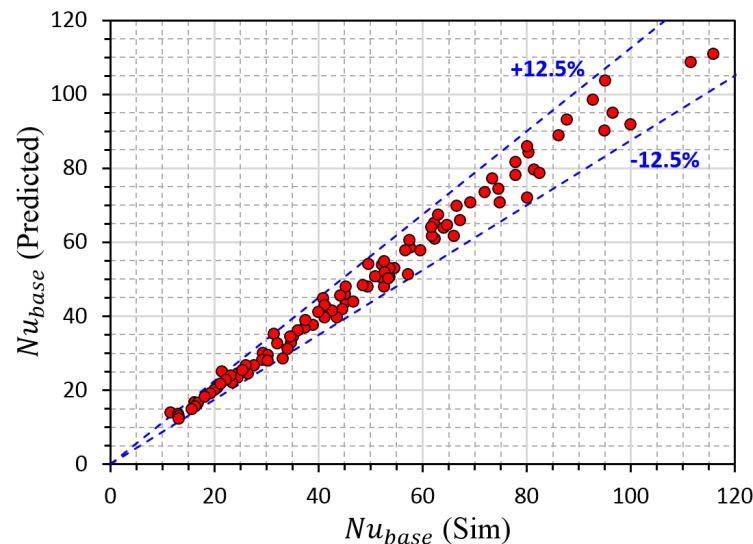


Figure 17. Comparison of predicted and simulated values of  $Nu_{base}$ .

Using a similar procedure, the correlations for  $Nu_{side}$  and  $f_{avg}$  were derived as Equations (26) and (27).

$$Nu_{side} = 0.01039 Re^{0.7946} (e/D)^{0.2762} (p/e)^{1.4995} \exp[-0.021[\ln(e/D)]^2] \exp[-0.2612[\ln(p/e)]^2] \quad (26)$$

$$f_{avg} = 12.989 Re^{-0.019} (e/D)^{4.1537} (p/e)^{1.233} \exp[0.5886[\ln(e/D)]^2] \exp[-0.2883[\ln(p/e)]^2] \quad (27)$$

Figure 18 compares the predicted values obtained using the developed correlations for  $Nu_{side}$  and  $f_{avg}$  with the CFD simulation results. The predicted values and CFD simulation results are in good agreement with MAPEs of 4.53 % and 7.33% for  $Nu_{side}$  and  $f_{avg}$ , respectively.

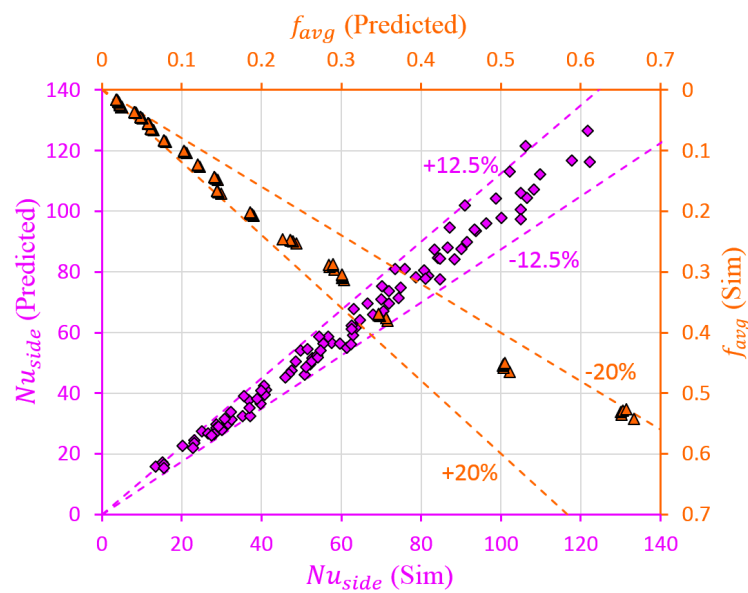


Figure 18. Comparison of predicted and simulated values of  $Nu_{side}$  and  $f_{avg}$ .

## 5. Conclusions

In the current investigation, CFD analysis has been conducted to examine the effects of rectangular ribs installed at the base and side surfaces of the fin in an SAH on the heat transfer enhancement and fluid flow characteristics. The key findings obtained in this research are as follows:

(1) The  $Nu_{avg}$  increased with an increase in  $Re$  for a given relative height and pitch. It also increased with increasing relative height of the rib for given  $Re$  and relative pitch. In addition, the  $Nu_{avg}$  tends to increase and then decrease as the relative pitch increases, and the optimal relative pitch ranged between 0.1 and 0.26 depending on the relative height of the rib and  $Re$ .

(2) The enhancement in  $Nu_{avg}$  varied from 1.19 to 3.497, and the maximum enhancement was found when the relative height, pitch, and  $Re$  were 0.28, 10, and 3000, respectively.

(3) The  $f_{avg}$  increased through the addition of a rectangular rib, and it raised with an increment in relative height, and a decrement in relative pitch, while it showed inconsiderable change with a change in  $Re$ .

(4) The enhancement in  $f_{avg}$  was in the range of 1.709 to 85.597, and the maximum  $f_{avg}$  was found when the relative height, pitch, and  $Re$  were 0.28, 10, and 15,000, respectively.

(5) The THP varied from 0.609 to 1.279 according to the geometric condition of the rib and  $Re$ . The maximum THP was found when the relative height, pitch, and  $Re$  were 0.10, 34, and 3000, respectively.

(6) The correlations for  $Nu_{base}$ ,  $Nu_{side}$ , and  $f_{avg}$  have been developed as a function of  $Re$ , relative height, and relative pitch of the rib. These correlations accurately predicted the values of  $Nu_{base}$ ,  $Nu_{side}$ , and  $f_{avg}$  with MAPEs of 4.24%, 4.53%, and 7.33%, respectively.

This study found that the addition of a rectangular rib to the fin surface provided an improvement in heat transfer between the fin surface and flowing air. Therefore, the feasibility of the ribbed fin could be confirmed. However, this study aims to examine how the rib attached to the fin affects heat transfer and pressure drop in an air channel of an SAH. Hence, future studies should be carried out to investigate the thermal efficiency improvement of an SAH by the proposed heat transfer device. The results and correlations obtained in this research are expected to provide valuable information for these further researches and the design of SAH.

**Author Contributions:** Conceptualization, H.-U.C. and K.-H.C.; methodology, H.-U.C.; software, H.-U.C., K.-A.M. and S.-B.K.; validation, H.-U.C. and K.-A.M.; data curation, H.-U.C., K.-A.M. and S.-B.K.; visualization, S.-B.K.; investigation, H.-U.C., S.-B.K. and K.-H.C.; writing—original draft

preparation, H.-U.C.; writing—review and editing, H.-U.C. and K.-H.C.; All authors have read and agreed to the published version of the manuscript.

**Funding:** This research received no external funding.

**Institutional Review Board Statement:** Not applicable.

**Informed Consent Statement:** Not applicable.

**Data Availability Statement:** Not applicable.

**Conflicts of Interest:** The authors declare no conflict of interest.

## Nomenclature

|                     |  |
|---------------------|--|
| $A$                 | Area (m <sup>2</sup> )                                     |
| $D$                 | Hydraulic diameter (m)                                     |
| $h$                 | Convective heat transfer coefficient (W/m <sup>2</sup> ·K) |
| $L$                 | Length (m)   |
| $\Delta P$          | Pressure drop (Pa)   |
| $\dot{Q}$           | Heat transfer rate (W)                                     |
| $T$                 | Temperature (°C)   |
| $V$                 | Velocity (m/s)   |
| $k$                 | Thermal conductivity (W/m·K)                               |
| $e$                 | Height of rectangular rib (m)                              |
| $p$                 | Pitch of rectangular rib (m)                               |
| $e/D$               | Relative height of rectangular rib (-)                     |
| $p/e$               | Relative pitch of rectangular rib (-)                      |
| $Nu$                | Nusselt number (-)   |
| $Re$                | Reynolds number (-)  |
| $Pr$                | Prandtl number (-)   |
| $f$                 | Friction factor (-)  |
| $f_g$               | Friction factor for Gnielinski correlation (-)             |
| <b>Greek symbol</b> |  |
| $\rho$              | Density (kg/m <sup>3</sup> )                               |
| <b>Subscript</b>    |  |
| $ac$                | Air channel  |
| $air$               | Air  |
| $avg$               | Average  |
| $base$              | Base surface of the fin                                    |
| $fin$               | Fin  |
| $s$                 | Smooth air channel   |
| $side$              | Side surface of the fin                                    |
| $tot$               | Total  |

## References

1. Chamoli, S.; Lu, R.; Xu, D.; Yu, P. Thermal Performance Improvement of a Solar Air Heater Fitted with Winglet Vortex Generators. *Sol. Energy* **2018**, *159*, 966–983. [[CrossRef](#)]
2. Markam, B.; Maiti, S. Artificial Enhancer for Small-Scale Solar Air Heater—A Comprehensive Review Aspect Ratio. *Clean. Energy Syst.* **2023**, *4*, 100046. [[CrossRef](#)]
3. Singh Bisht, V.; Kumar Patil, A.; Gupta, A. Review and Performance Evaluation of Roughened Solar Air Heaters. *Renew. Sustain. Energy Rev.* **2018**, *81*, 954–977. [[CrossRef](#)]
4. Yadav, A.S.; Bhagoria, J.L. A CFD (Computational Fluid Dynamics) Based Heat Transfer and Fluid Flow Analysis of a Solar Air Heater Provided with Circular Transverse Wire Rib Roughness on the Absorber Plate. *Energy* **2013**, *55*, 1127–1142. [[CrossRef](#)]
5. Yadav, A.S.; Bhagoria, J.L. A Numerical Investigation of Square Sectioned Transverse Rib Roughened Solar Air Heater. *Int. J. Therm. Sci.* **2014**, *79*, 111–131. [[CrossRef](#)]
6. Yadav, A.S.; Bhagoria, J.L. A CFD Based Thermo-Hydraulic Performance Analysis of an Artificially Roughened Solar Air Heater Having Equilateral Triangular Sectioned Rib Roughness on the Absorber Plate. *Int. J. Heat Mass Transf.* **2014**, *70*, 1016–1039. [[CrossRef](#)]

7. Gawande, V.B.; Dhoble, A.S.; Zodpe, D.B.; Chamoli, S. Experimental and CFD Investigation of Convection Heat Transfer in Solar Air Heater with Reverse L-Shaped Ribs. *Sol. Energy* **2016**, *131*, 275–295. [[CrossRef](#)]
8. Singh, A.; Singh, S. CFD Investigation on Roughness Pitch Variation in Non-Uniform Cross-Section Transverse Rib Roughness on Nusselt Number and Friction Factor Characteristics of Solar Air Heater Duct. *Energy* **2017**, *128*, 109–127. [[CrossRef](#)]
9. Singh, I.; Vardhan, S.; Singh, S.; Singh, A. Experimental and CFD Analysis of Solar Air Heater Duct Roughened with Multiple Broken Transverse Ribs: A Comparative Study. *Sol. Energy* **2019**, *188*, 519–532. [[CrossRef](#)]
10. Choi, H.U.; Choi, K.H. CFD Analysis on the Heat Transfer and Fluid Flow of Solar Air Heater Having Transverse Triangular Block at the Bottom of Air Duct. *Energies* **2020**, *13*, 1099. [[CrossRef](#)]
11. Kumar, R.; Goel, V. Unconventional Solar Air Heater with Triangular Flow-Passage: A CFD Based Comparative Performance Assessment of Different Cross-Sectional Rib-Roughnesses. *Renew. Energy* **2021**, *172*, 1267–1278. [[CrossRef](#)]
12. Alam, M.W.; Souayeh, B. Parametric CFD Thermal Performance Analysis of Full, Medium, Half and Short Length Dimple Solar Air Tube. *Sustainability* **2021**, *13*, 6462. [[CrossRef](#)]
13. Haldar, A.; Varshney, L.; Verma, P. Effect of Roughness Parameters on Performance of Solar Air Heater Having Artificial Wavy Roughness Using CFD. *Renew. Energy* **2022**, *184*, 266–279. [[CrossRef](#)]
14. Singh, V.P.; Jain, S.; Karn, A.; Kumar, A.; Dwivedi, G.; Meena, C.S.; Cozzolino, R. Mathematical Modeling of Efficiency Evaluation of Double-Pass Parallel Flow Solar Air Heater. *Sustainability* **2022**, *14*, 10535. [[CrossRef](#)]
15. Fakoor Pakdaman, M.; Lashkari, A.; Basirat Tabrizi, H.; Hosseini, R. Performance Evaluation of a Natural-Convection Solar Air-Heater with a Rectangular-Finned Absorber Plate. *Energy Convers. Manag.* **2011**, *52*, 1215–1225. [[CrossRef](#)]
16. Fudholi, A.; Sopian, K.; Ruslan, M.H.; Othman, M.Y. Performance and Cost Benefits Analysis of Double-Pass Solar Collector with and without Fins. *Energy Convers. Manag.* **2013**, *76*, 8–19. [[CrossRef](#)]
17. Yang, M.; Yang, X.; Li, X.; Wang, Z.; Wang, P. Design and Optimization of a Solar Air Heater with Offset Strip Fin Absorber Plate. *Appl. Energy* **2014**, *113*, 1349–1362. [[CrossRef](#)]
18. Priyam, A.; Chand, P. Thermal and Thermohydraulic Performance of Wavy Finned Absorber Solar Air Heater. *Sol. Energy* **2016**, *130*, 250–259. [[CrossRef](#)]
19. Kabeel, A.E.; Hamed, M.H.; Omara, Z.M.; Kandeal, A.W. Influence of Fin Height on the Performance of a Glazed and Bladed Entrance Single-Pass Solar Air Heater. *Sol. Energy* **2018**, *162*, 410–419. [[CrossRef](#)]
20. Kansara, R.; Pathak, M.; Patel, V.K. Performance Assessment of Flat-Plate Solar Collector with Internal Fins and Porous Media through an Integrated Approach of CFD and Experimentation. *Int. J. Therm. Sci.* **2021**, *165*, 106932. [[CrossRef](#)]
21. Chand, S.; Chand, P.; Kumar Ghritlahre, H. Thermal Performance Enhancement of Solar Air Heater Using Louvered Fins Collector. *Sol. Energy* **2022**, *239*, 10–24. [[CrossRef](#)]
22. Nagaraj, M.; Reddy, M.K.; Honnesara Sheshadri, A.K.; Karanth, K.V. Numerical Analysis of an Aerofoil Fin Integrated Double Pass Solar Air Heater for Thermal Performance Enhancement. *Sustainability* **2023**, *15*, 591. [[CrossRef](#)]
23. Singh, S.; Singh, B.; Hans, V.S.; Gill, R.S. CFD (Computational Fluid Dynamics) Investigation on Nusselt Number and Friction Factor of Solar Air Heater Duct Roughened with Non-Uniform Cross-Section Transverse Rib. *Energy* **2015**, *84*, 509–517. [[CrossRef](#)]
24. Singh, I.; Singh, S. CFD Analysis of Solar Air Heater Duct Having Square Wave Profiled Transverse Ribs as Roughness Elements. *Sol. Energy* **2018**, *162*, 442–453. [[CrossRef](#)]
25. Kumar, R.; Kumar, A.; Goel, V. Performance Improvement and Development of Correlation for Friction Factor and Heat Transfer Using Computational Fluid Dynamics for Ribbed Triangular Duct Solar Air Heater. *Renew. Energy* **2019**, *131*, 788–799. [[CrossRef](#)]
26. Kumar, A.; Saini, R.P.; Saini, J.S. Experimental Investigation on Heat Transfer and Fluid Flow Characteristics of Air Flow in a Rectangular Duct with Multi V-Shaped Rib with Gap Roughness on the Heated Plate. *Sol. Energy* **2012**, *86*, 1733–1749. [[CrossRef](#)]
27. Nidhul, K.; Yadav, A.K.; Anish, S.; Arunachala, U.C. Efficient Design of an Artificially Roughened Solar Air Heater with Semi-Cylindrical Side Walls: CFD and Exergy Analysis. *Sol. Energy* **2020**, *207*, 289–304. [[CrossRef](#)]
28. Patel, S.S.; Lanjewar, A. Experimental Investigation of Solar Air Heater Duct with Discrete V-Rib Integrated with Staggered Elements. *Int. J. Sustain. Eng.* **2021**, *14*, 162–171. [[CrossRef](#)]
29. Kumar, S.; Verma, S.K. Heat Transfer and Fluid Flow Analysis of Sinusoidal Protrusion Rib in Solar Air Heater. *Int. J. Therm. Sci.* **2022**, *172*, 107323. [[CrossRef](#)]
30. Chaube, A.; Sahoo, P.K.; Solanki, S.C. Analysis of Heat Transfer Augmentation and Flow Characteristics Due to Rib Roughness over Absorber Plate of a Solar Air Heater. *Renew. Energy* **2006**, *31*, 317–331. [[CrossRef](#)]
31. Alam, T.; Kim, M.H. Heat Transfer Enhancement in Solar Air Heater Duct with Conical Protrusion Roughness Ribs. *Appl. Therm. Eng.* **2017**, *126*, 458–469. [[CrossRef](#)]
32. Cengel, Y.A.; Ghajar, A.J. *Heat and Mass Transfer: Fundamentals & Applications*, 4th ed.; McGraw-Hill: New York, NY, USA, 2011.
33. Webb, R.L.; Eckert, E.R.G. Application of Rough Surfaces to Heat Exchanger Design. *Int. J. Heat Mass Transf.* **1972**, *15*, 1647–1658. [[CrossRef](#)]
34. Gupta, A.D.; Varshney, L. Performance Prediction for Solar Air Heater Having Rectangular Sectioned Tapered Rib Roughness Using CFD. *Therm. Sci. Eng. Prog.* **2017**, *4*, 122–132. [[CrossRef](#)]
35. Karwa, R.; Chauhan, K. Performance Evaluation of Solar Air Heaters Having V-down Discrete Rib Roughness on the Absorber Plate. *Energy* **2010**, *35*, 398–409. [[CrossRef](#)]
36. Matheswaran, M.M.; Arjunan, T.V.; Somasundaram, D. Analytical Investigation of Solar Air Heater with Jet Impingement Using Energy and Exergy Analysis. *Sol. Energy* **2018**, *161*, 25–37. [[CrossRef](#)]

37. Choi, H.; Choi, K. Parametric Study of a Novel Air-Based Photovoltaic-Thermal Collector with a Transverse Triangular-Shaped Block. *Renew. Energy* **2022**, *201*, 96–110. [[CrossRef](#)]
38. Singh, V.P.; Jain, S.; Karn, A.; Kumar, A.; Dwivedi, G.; Meena, C.S.; Dutt, N.; Ghosh, A. Recent Developments and Advancements in Solar Air Heaters: A Detailed Review. *Sustainability* **2022**, *14*, 12149. [[CrossRef](#)]

**Disclaimer/Publisher's Note:** The statements, opinions and data contained in all publications are solely those of the individual author(s) and contributor(s) and not of MDPI and/or the editor(s). MDPI and/or the editor(s) disclaim responsibility for any injury to people or property resulting from any ideas, methods, instructions or products referred to in the content.